Remote Sensing of Environment 295 (2023) 113652

Contents lists available at ScienceDirect

Remote Sensing of Environment

journal homepage: www.elsevier.com/locate/rse

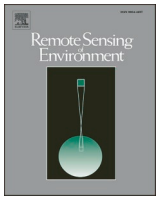

Improving quantification of methane point source emissions from imaging spectroscopy

Zhipeng Pei [a,c], Ge Han [b,f,*], Huiqin Mao [d], Cuihong Chen [d], Tianqi Shi [a], Keyi Yang [b], Xin Ma [a], Wei Gong [a,e]

[a] State Key Laboratory of Information Engineering in Surveying, Mapping and Remote Sensing, Wuhan University, Wuhan, China
[b] School of Remote Sensing and Information Engineering, Wuhan University, Wuhan, China
[c] Hubei Luojia Laboratory, Wuhan, China
[d] Ministry of Ecology and Environment Center for Satellite Application on Ecology and Environment/ State Environmental Protection Key Laboratory of Satellite Remote Sensing, Beijing, China
[e] Wuhan Institute of Quantum Technology, Wuhan, China
[f] Perception and Effectiveness Assessment for Carbon-neutral Efforts, Engineering Research Center of Ministry of Education, Wuhan, China

ARTICLE INFO

Keywords:
Imaging spectrometer
Methane emission
Detection methods
Gas retrieval
Point sources
Gas plume
PRISMA

ABSTRACT

The matched filter (MF) method is widely used for hyperspectral imaging spectrometers to detect and quantify methane point sources due to its high computational efficiency. However, it would result in an unavoidable underestimation, especially for large concentration enhancements. The lognormal matched filter (LMF) has provided a unique and not limited to weak methane plumes theory through lognormal background radiances modeling, but validations on simulated experiments and applications to real data remain to be explored. Moreover, the covariance contamination caused by the enhanced pixels and the surface heterogeneity have detrimental effects on the detection methods for real data application. In this study, we propose the iterative lognormal matched filter (ILMF) method to address these challenges. We evaluate the performance of the ILMF with two ideal simulations and the end-to-end simulation. The results of random simulated enhancement retrievals show that the retrieved enhancement by the ILMF method agrees well with the true enhancement, with an R^2 of 0.984 and a small root-mean-square error (RMSE) of 55.856 ppb. The ILMF method reduce the RMSE of retrieved enhancement by 80% compared with the MF method. The results of end-to-end simulations show the underestimation of MF method at different sites regarding the emission rate, as well as the improvement of the ILMF method. Further, we apply the ILMF method to detect and quantify point sources in some methane hotspot regions. Our study reports the underestimation in traditional MF method and provides an unbiased and robust method for quantifying methane emissions.

1. Introduction

Methane is a potent greenhouse gas that is responsible for approximately 30% of global warming since pre-industrial times (Naik et al., 2021), second only to carbon dioxide (CO_2) in driving climate change (Masson-Delmotte et al., 2021). Methane has a global warming potential (GWP) that is >80 times greater than CO_2 over 20-year period (EPA, 2022). The fossil fuel industry, including oil and gas (O&G) extraction and coal mining, accounts for approximately 35% of global anthropogenic methane emissions (UNEP and CCAC, 2021). Therefore, reducing methane emissions from industrial activities is considered to be the fastest and the most impactful solution for addressing near-term climate warming. However, detecting a large number of emission point sources (Duren et al., 2019) with relatively small sizes worldwide is particularly challenging since they often occur unexpectedly (Cusworth et al., 2021a), such as in pipeline leaks, facility failures. Furthermore, the quantity, duration, and frequency of leaks may vary considerably across regions and time periods (Irakulis-Loitxate et al., 2021, 2022). Regular monitoring of these methane emitters with high spatial resolution and high frequency is therefore essential and a prerequisite for cutting methane emissions (Chen et al., 2022).

Methane has fundamental vibrational absorptions in the shortwave infrared (SWIR) spectrum. Satellites that measure reflected solar radiation in the SWIR can detect subtle signal variations due to the methane

* Corresponding author at: School of Remote Sensing and Information Engineering, Wuhan University, Wuhan, China.
E-mail address: udhan@whu.edu.cn (G. Han).

https://doi.org/10.1016/j.rse.2023.113652
Received 16 April 2023; Received in revised form 19 May 2023; Accepted 24 May 2023
Available online 12 June 2023

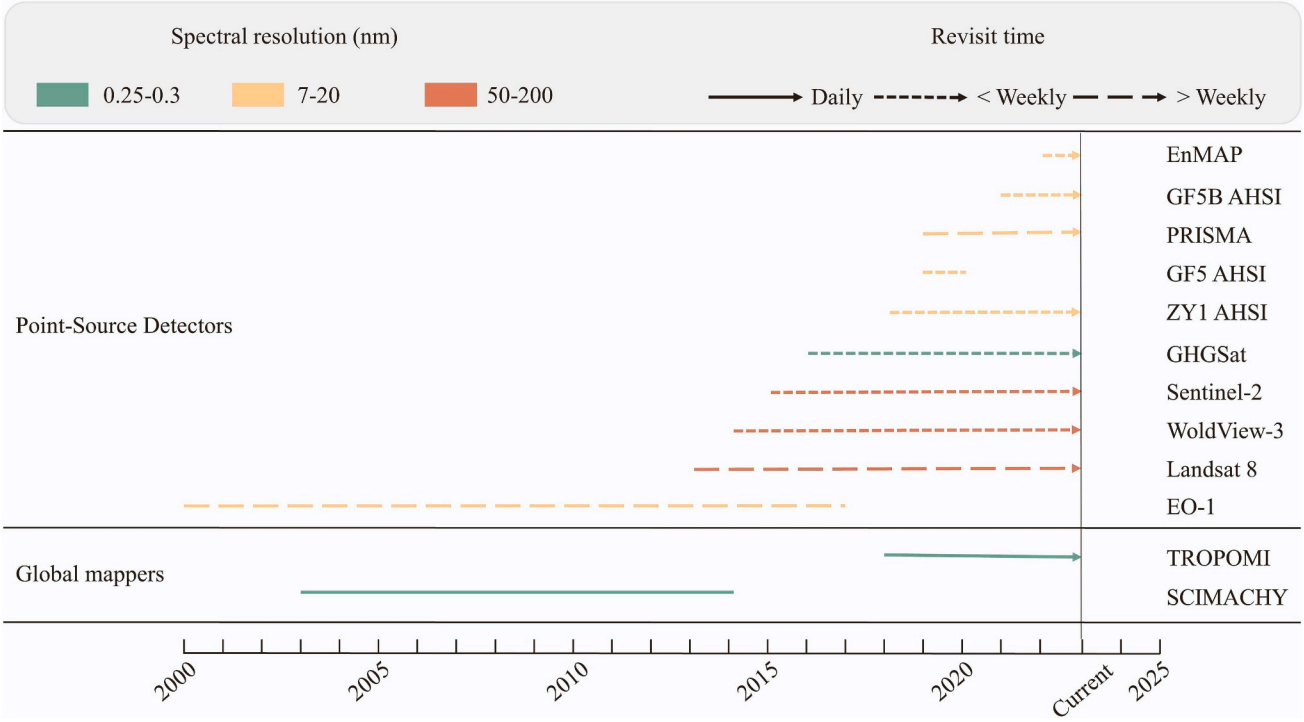

Fig. 1. Description of satellites that can be used for methane detection, including operational time, revisit period, spectral resolution, and spatial resolution.

absorption. This provides a great capability for monitoring point sources globally and individually (Frankenberg et al., 2005a; Jacob et al., 2016, 2022). However, given the mutual constraints of the high spatial resolution and the high frequency, satellites with different designs are required to collaborate to investigate methane point sources on a global scale (see Fig. 1) (Varon et al., 2021). Global mappers such as SCIMACHY (30×60 km^2 pixels) and TROPOMI (5.5×7 km^2 pixels) can provide daily methane column concentration (XCH_4). However, their limited spatial resolution means that we are unable to finely localize individual emission sources and distinguish their respective contributions (Sadavarte et al., 2021). Complementary to global mappers, some hyperspectral and multispectral missions are gradually demonstrating their capabilities to map plumes and to quantify emission rates for individual methane point sources. Imaging spectrometers measuring radiation at approximately 10 nm spectral sampling with 30 m spatial sampling, such as EO-1 Hyperion (Thompson et al., 2016), ZY1 AHSI (Irakulis-Loitxate et al., 2021), PRISMA (Guanter et al., 2021) and GF5 AHSI (Irakulis-Loitxate et al., 2021), have shown great potential for methane mapping in O&G producing and coal mining regions. Recent studies have demonstrated the capability of multispectral satellites, including Landsat 5/8 (Irakulis-Loitxate et al., 2022), Sentinel 2 (Varon et al., 2021; Gorroño et al., 2022; Ehret et al., 2022) and WorldView 3 (Sánchez-Garca et al., 2022), to detect methane plumes with a high spatial resolution and a frequent revisit. The commercial GHGSat constellation (Jervis et al., 2021; Ramier et al., 2020) is specifically designed to detect methane point sources with a high spatial resolution (25 m or 50 m) and a high precision ($\sim$ 1%–15%) for targeting $\sim 10 \times 10$ km^2 domains. The collaboration of satellites with different designs will be an important means of detecting methane point sources on a global scale. TROPOMI-like satellites can help highlight regions that have large methane leaks, while PRISMA-like satellites with a high spatial resolution can precisely locate and quantify methane point sources in target areas. Regular monitoring is particularly effective for detecting strong point source emissions and has great potential to help environmental authorities to regulate unknown methane emitters.

Physically-based methods, including WFM-DOAS (Buchwitz and

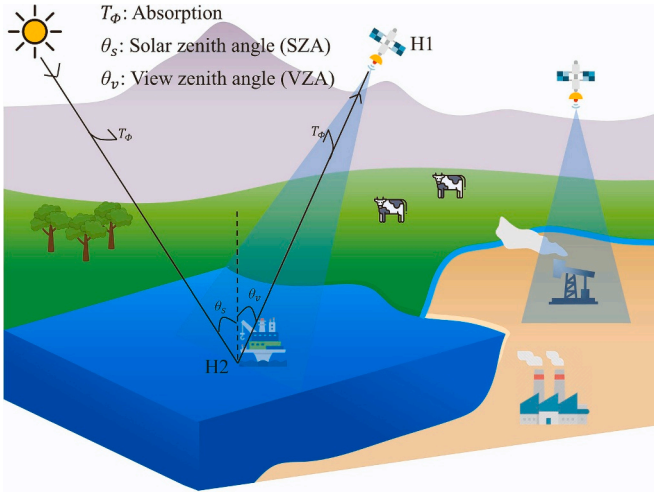

Fig. 2. Satellite observation schematic of methane point sources detection.

Burrows, 2004) and IMAP-DOAS (Frankenberg et al., 2005b; Thorpe et al., 2014), retrieve some parameters relying on explicit radiative transfer modeling. Alternatively, data-driven methods improve the computational efficiency by simplifying complicated atmospheric radiative transfer models, such as the band ratio (BR) method (Roberts et al., 2010; Bradley et al., 2011; Scafutto et al., 2021), and the matched filter (MF) method (Thompson et al., 2016; Dennison et al., 2013; Thorpe et al., 2013). Among them, the MF method has been widely used (Thorpe et al., 2016; Frankenberg et al., 2016; Cusworth et al., 2021b; Foote et al., 2020; Cusworth et al., 2020, 2021a; Zhang et al., 2023) in airborne and spaceborne experiments as it enables methane column concentration enhancement (ΔXCH_4) mapping and further estimating emission rates (in kg/h), based on the Taylor's expansion simplification and a linear least squares fit. However, the MF method is limited by its simplified linear signal model and may not fully capture the physical processes involved in gas detection, particularly in the case of strong

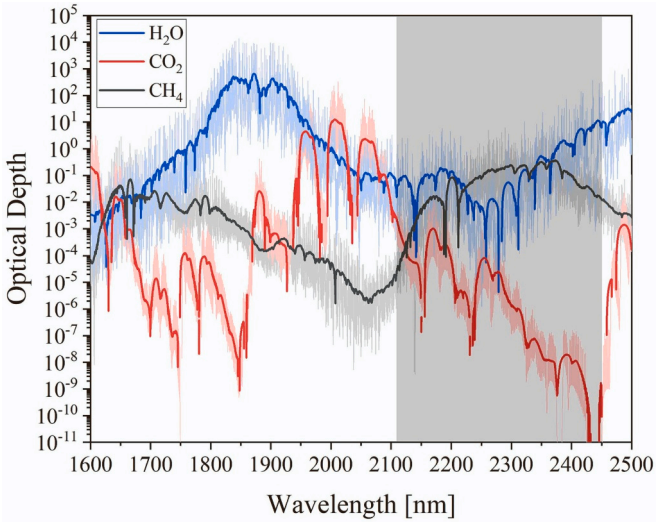

Fig. 3. Vertical optical depths of water vapor, carbon dioxide and methane in the 1600–2500 nm spectral range. Absorption line parameters are based on the HITRAN database. The values are for the 1976 U.S. Standard Atmosphere (Anderson et al., 1986) with a solar zenith angle (SZA) of 0° and viewing zenith angle (VZA) of 0°. Lighter colors are original optical depths sampled at 0.1 cm^{-1} spectral resolution, and darker colors are optical depths smoothed by the Savitzsky-Golay filter.

plumes (Schaum, 2021). Due to the linear approximation, only the concentration of weak plumes can be derived accurately, while stronger plumes tend to be underestimated. To address this fundamental problem, the lognormal matched filter (LMF) method has been proposed, which provides a theoretically optimal solution for all gas concentrations, including strong plumes.

Moreover, the unit methane absorption coefficient (k) is a key parameter for both MF and LMF methods, directly affecting the concentration enhancement retrieval. It represents the total optical depth increment resulting from per unit concentration methane, which is affected by the solar zenith angle (SZA), the view zenith angle (VZA), the sensor height (H1), and the surface elevation (H2) at the time of observation (see Fig. 2). To retrieve the concentration enhancement from a given satellite, it is necessary to determine the convolved k that corresponds to its spectral resolution and sampling.

This paper is organized as follows. In Sect. 2, the MF and the LMF theories and the procedure for calculating k considering two-way absorption are described in detail. Then we propose an Iterative Lognormal Matched Filter (ILMF) method to overcome the covariance contamination caused by the enhanced pixels. Sect. 3 demonstrates the advantages of ILMF over LMF and MF by simulation results and presents some examples of methane plumes retrieved by the ILMF method using real PRISMA data. This work is motivated by PRISMA-like hyperspectral satellites but is generally applicable to Sentinel 2-like multispectral satellites.

2. Materials and methods

2.1. ΔXCH_4 retrieval methods

Methane, water vapor and carbon dioxide have fundamental vibrational absorptions in the SWIR spectrum. Fig. 3 shows modeled atmospheric optical depths for these three major greenhouse gases. These atmospheric optical depths were generated using the HAPI tool based on the HITRAN database (Kochanov et al., 2016). The strongest methane absorptions peak at approximate wavelengths of 1650 and 2300 nm. Methane absorption features overlap with the other two interference gases. By comparisons, the methane absorption feature near 2300 nm is less susceptible to the interference from other gases and is therefore often chosen as the retrieval window.

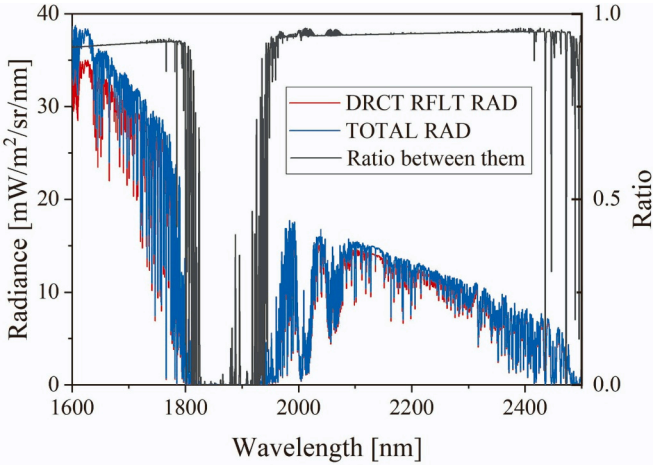

Fig. 4. Comparision between the direct reflected solar radiance (DRCT RFLT RAD) and the total radiance (TOTAL RAD). These radiances are simulated by the MODTRAN model. The solid black line is the ratio between them.

The basic principle of the ΔXCH_4 retrieval methods is to use the difference between radiances to calculate the concentration enhancement compared to the methane-free pixels. The clear sky top of atmosphere upwelling radiance is composed of radiances emitted by the surface, radiances reflected by the surface, and radiances emitted by the atmosphere (Saunders et al., 1999). Fig. 4 shows the direct reflected solar radiance from the surface (DRCT RFLT RAD), the total radiance (TOTAL RAD) and the ratio between them. The simulated solar radiance pass through all layers in both the downwelling and the upwelling direction. In this study, the reflected radiance accounts for >95% of the total radiance for the methane retrieval window (~2110–2450 nm). Thus, the calculation of the unit methane absorption coefficient must take into account the two-way absorption. These radiances are obtained from the 1976 U.S. Standard Atmosphere (Anderson et al., 1986), surface temperature of 300 K, and surface albedo of 0.5. Several detection methods will be described below.

2.1.1. Matched filter

It is assumed that the SWIR radiance spectrum received by satellite sensors satisfies a normal distribution ($x \sim \mathcal{N}(x_r, \Sigma)$) for methane-free pixels over homogeneous surfaces. Assuming that the methane concentration enhancement is only present in a very small number of pixels, the reference spectrum x_r and the covariance matrix Σ can be estimated with the background pixels spectrum (x_b).

$$x_r \approx \frac{1}{N}\sum_{n=1}^{N} x_b(n), \qquad \Sigma \approx \frac{1}{N}\sum_{n=1}^{N}[x_b(n) - x_r][x_b(n) - x_r]^T \tag{1}$$

where N is the number of background pixels. To avoid the effect of the strip noise, x_r and Σ are calculated on a per-column basis.

According to Beer Lambert's law, the spectrum which is affected by the methane concentration enhancement can be modeled as,

$$x_m = x_r e^{-k\Delta c}, \tag{2}$$

where x_r is the reference spectrum which is not affected by the methane concentration enhancement and Δc is the methane concentration enhancements. And the detailed calculation procedure to deduce k is described in Sect. 2.3. The estimation of Δc is typically based on fitting the observed spectrum (x_o) and modeled spectrum (x_m) in the SWIR

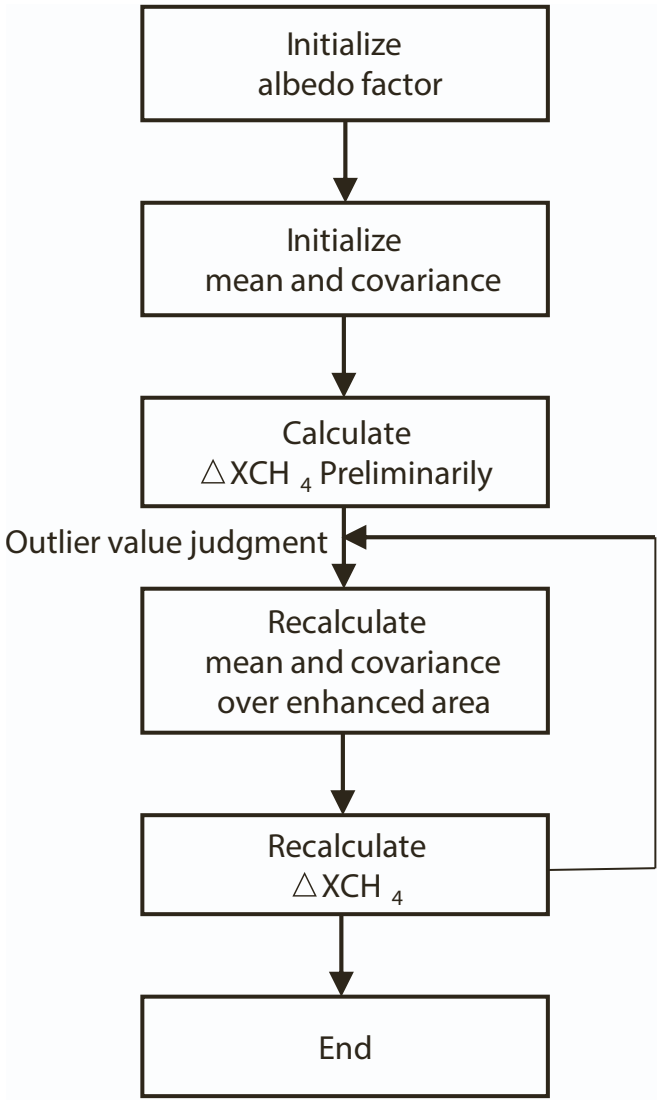

Fig. 5. Flow chart of ILMF method.

spectral region. Modeled spectrum can be linearized according to the first-order Taylor expansion,

$$x_m = x_r(1 - k\Delta c). \tag{3}$$

Further, the goal is to minimize the residuals between the observed and modeled spectrums, as shown in Eq. (4).

$$\sum_{i=1}^{I} \left(x_o^i - x_m^i\right)^2 \equiv \| \text{RES}\|^2 \rightarrow min, \tag{4}$$

where I is the number of bands in the retrieval window (2110–2450 nm). Its least squares solution can be expressed as

$$\begin{aligned} \Delta c &= \left((x_r k)^T \Sigma^{-1}(x_r k)\right)^{-1}(x_r k)^T \Sigma^{-1}(x_r - x_t) \\ &= \frac{(x_r k)^T \Sigma^{-1}(x_r - x_t)}{(x_r k)^T \Sigma^{-1}(x_r k)} \end{aligned} \tag{5}$$

It is worth noting that the linearization in Eq. (1) only applies to the case of weak methane plume with small Δc (Schaum, 2021). The retrieval result will be unfaithful for large Δc. Although such linearization does not affect the detection of methane point sources, it does affect the subsequent quantification of emission rates.

2.1.2. Lognormal matched filter

As a means of addressing the shortcomings associated with the MF method, it has been proposed that the lognormal distribution can be utilized as an alternative spectral background model (Schaum, 2021). The normal distribution adapted to negative unphysical electro-optic signals while the logarithmic distribution supports only positive ones. Taking logarithms for both sides of Eq. (1),

$$ln(x_m) = ln(x_r) - k\Delta c \tag{6}$$

Since the background is assumed to be log-normally distributed, the residuals ($V = ln(x_m) - ln(x_o)$) are considered to satisfy a normal distribution. The fundamental result of LMF detector can be expressed as,

$$\Delta c = \frac{k^T \Sigma^{-1}(ln(x_r) - ln(x_t))}{k^T \Sigma^{-1} k}, \tag{7}$$

where

$$\begin{aligned} ln(x_r) &\approx \frac{1}{N}\sum_{n=1}^{N} ln(x_b(n)), \\ \Sigma &\approx \frac{1}{N}\sum_{n=1}^{N} [ln(x_b(n)) - x_r][ln(x_b(n)) - x_r]^T. \end{aligned} \tag{8}$$

The unit methane absorption coefficient used in the LMF method is consistent with that in the MF method and will be described in detail in the Sec. 2.2.

2.1.3. Iterative lognormal matched filter

The estimation of the mean and the covariance is crucial for both MF and LMF, as shown in Eq. (1) and Eq. (8), respectively. These values are not reliable for images with a large proportion of enhanced pixels. In particular, the "contaminated" covariance matrix can introduce large errors into the results.

Iterative matched filter (Kim et al., 2016; Foote et al., 2020) allows updating the mean and the covariance matrix, which can effectively reduce the contamination of background statistics by target signals. In this study, we proposed the iterative lognormal matched filter (ILMF) method to update the mean and the covariance by eliminating the pixels initially judged enhanced. The specific flow chart using ILMF for this study is shown in Fig. 5. The outliers are considered statistically significant ΔXCH_4 which exceed twice the level of noise (2σ threshold, $p < 0.05$). The iterations terminate when there are no outliers in the ΔXCH_4 or when the number of iterations exceeds five. Subsequently, we update the mean and the covariance for the final time.

2.2. Effect of surface type

The presence of multiple surface types within a scene can introduce a variability in the reflected signal, leading to errors in the estimation of the methane plume. This is because different surface types have different reflectance properties in the SWIR region, which can affect the accuracy of the mean and the covariance estimation. A bright and homogeneous surface is ideal for accurate estimation of the methane plume, as it facilitates a better estimation of the mean and the covariance. In contrast, a heterogeneous and relatively dark surface is unfavorable for methane plume detection. Even though the negative effect due to heterogeneity can theoretically be eliminated as much as possible by clustering the surface types, the actual clustering effect in complex regions needs further study. How to choose a clustering method is beyond the scope of this study. Our results also revealed that certain surface types possess distinct absorption characteristics, such as those found in vegetable trellises, painted soccer fields, and photovoltaic panels (see Supplement), which result in erroneous classification as enhanced pixels by the MF or ILMF. These false positives necessitate additional visual interpretation, taking into account wind direction and high-resolution optical images to accurately distinguish them.

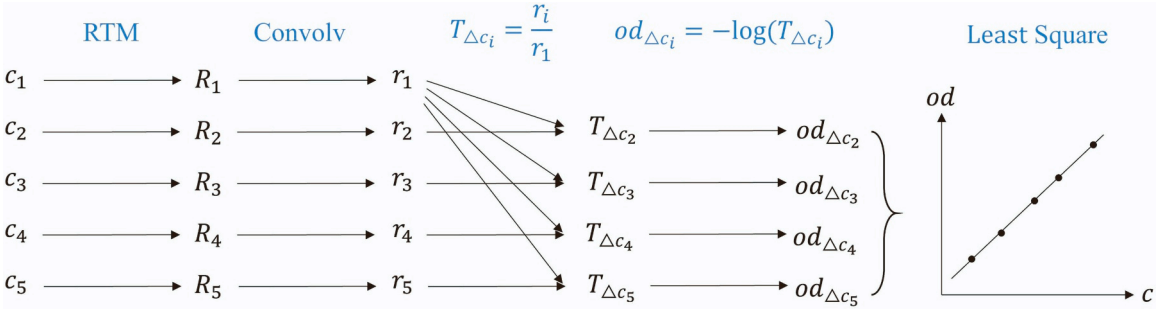

Fig. 6. Flow chart of unit methane absorption coefficient calculation procedure.

In addition, sensor noise comes from two main components: the photonic noise and the constant noise (Ayasse et al., 2019). Thus, the measured signal-to-noise ratio (SNR) decreases for darker surfaces. Further, the retrieval precision decreases for low radiances due to large solar zenith angles or dark surfaces.

For a retrieval over a single pixel, a reference spectrum for that pixel is required. Retrieval errors may occur when an albedo-influenced reference spectrum is used, if the overall brightness of a pixel deviates from the average brightness in the across-track direction. This effect can be compensated by overall scaling of the spectrum with an albedo factor (Foote et al., 2020) For example, darker pixels correspond to albedo factors >1. We applied this idea in the ILMF method.

2.3. Calculation procedure of unit methane absorption coefficient

The unit methane absorption coefficient is determined by both the optical path length and the methane absorption cross section. In other words, it represents the total optical depth variation for a unit of methane concentration. Unlike the airborne experiments (Frankenberg et al., 2016; Thompson et al., 2015), the sensor is higher for spaceborne observations. For a given satellite (e.g., PRISMA), it is necessary to determine the convolved k that corresponds to its spectral features (resolution and sampling). Specifically, the procedure for calculating k is as follows. The corresponding flow chart is shown in Fig. 6.

1) Given five atmospheric profiles (including temperature, pressure, and volume mixing ratio of various gases), the only difference between them is the methane concentration. The column concentrations of methane are noted as c_1 to c_5 in an ascending order.
2) The high resolution radiances corresponding to the different concentrations was calculated by the radiative transfer model (RTM).
3) The Gaussian spectral response function is used to generate convolved radiances for a given satellite, which is determined by the central wavelength and full width at half maxima (FWHM). The convolved radiances corresponding to c_1 to c_5 are noted as r_1 to r_5.
4) Regarding c_1 as the background column concentration, the difference between c_2 to c_5 and c_1 is noted as Δc_2 to Δc_5. The transmittance due to methane absorption corresponding to Δc_2 to Δc_5 can be obtained from the convolved radiances as $T_{\Delta_{c_i}} = \frac{r_i}{r_1}$.
5) Further, the optical depth increment due to the methane enhancement can be expressed as $od_{c_i} = -ln\left(T_{\Delta_{c_i}}\right)$.
6) Lastly, the coordinates of the four points $(\Delta c_i, od_{\Delta c_i})$ were used for the least squares fitting. The obtained slope is the unit methane absorption coefficient.

It is noteworthy that there are several underlying assumptions in this section about atmospheric profiles that affect the slope of the fitting.

2.4. Three image-level simulations

In this study, we employ three sets of simulated hyperspectral data as input for the retrieval of methane concentration enhancement. Table 1 provides an overview of the three sets of simulations, including the methods used for ΔXCH_4 maps generation, surface variations, and instrument precision (σ). The total concentration, comprising of the generated ΔXCH_4 and the background concentration, can be used as input to the radiative transfer model (RTM) to generate the radiance or transmittance. Considering the global average column concentration of methane in recent years and the increasing trend (Jacob et al., 2022; Zhang et al., 2022; Yang et al., 2023), the background concentration is assumed to be 1900 ppb in this study. In the Simulation 1, 2% of the pixels are randomly selected and enhanced with uniformly random value from 1 to 1500 ppb. In the Simulation 2–3, concentration enhancement images are generated by the WRF-LES model. Simulation 3 contains the surface variation and the noise of the real PRISMA data, also known as end-to-end simulation. Similar to Cusworth et al. (2019) and Guanter et al. (2021), the effect of the simulated plume is added to the real PRISMA TOA images without plumes for generating pseudo-observations. The high-resolution transmittance spectra generated by WRF-LES are convolved by the spectral response function of PRISMA and then are multiplied with the real PRISMA TOA spectrum. Compared with the simulation 2, the end-to-end simulation is more challenging for the plume retrieval, due to a large instrument noise, heterogeneous surfaces, instrumental artifacts, and potential false positives. Plumes caused by small emission rates may be invisible in end-to-end simulations, as small concentration enhancements can be drowned out by noise. Additionally, end-to-end simulations can be used to investigate the performance of retrieval methods in different places of the world. We selected four subsets of the real PRISMA TOA images from four locations in Algeria, Turkmenistan, China, and the United States, as shown in Fig. 7. The selection of these four locations is driven by their distinct surface characteristics in terms of heterogeneity and brightness, as well as their prominent role in the energy industry (Varon et al., 2021; Guanter et al., 2021), which leads to the release of significant amounts of methane into the atmosphere. We chose these four images with similar SZA in order to minimize the effect of the SZA on the results. Fig. 7 shows the true-colour composite images of the four selected subsets (100 × 100 pixel) containing the plume and the TOA radiance at 2300 nm.

Table 1
Description of the three image-level simulations.

	ΔXCH_4 generation	Surface variation	Instruments precision
Simulation 1	Uniformly random value	Not considered	1%
Simulation 2	WRF-LES	Not considered	1%
Simulation 3	WRF-LES	True data from PRISMA	True data from PRISMA

The concentration enhancement can be retrieved using noised pseudo-observations to investigate the performance of different ΔXCH_4

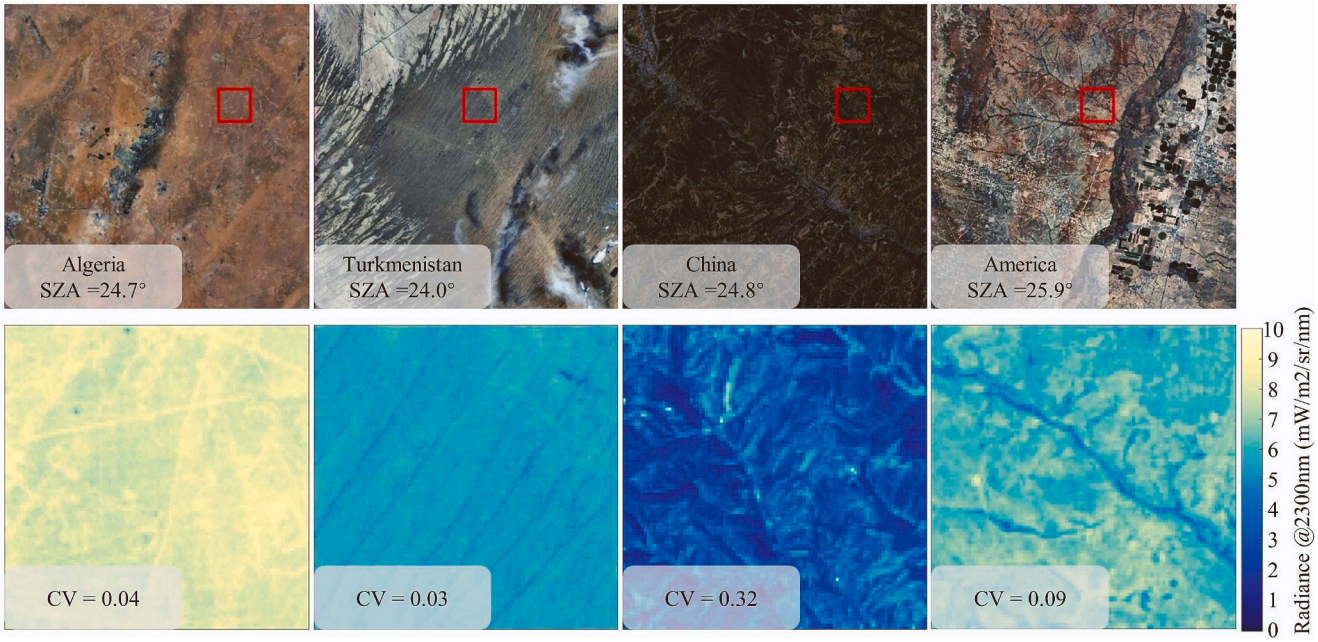

Fig. 7. Real PRISMA TOA data for the end-to-end simulations in this study. Top row, true colour composites of the three PRISMA images (1000 × 1000 pixels). The red squares represents the location of the 100 × 100 pixels subsets where simulated methane plumes are included. Bottom row, TOA radiance map at 2300 nm for the 100 × 100 subsets in the red squares of the top row. CV in the label on the bottom left corner of each panel refers to the coefficient of variation (standard deviation over mean) of radiance at 2300 nm within the image. (For interpretation of the references to colour in this figure legend, the reader is referred to the web version of this article.)

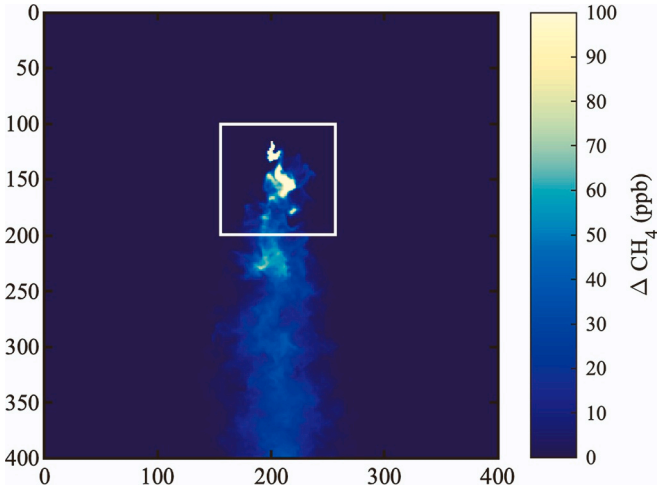

Fig. 8. Simulated concentration enhancement image for 30 m spatial resolution with an emission rate of 2000 kg/h by WRF-LES. The plume in the white boxes (100 × 100 pixels) are for end-to-end simulation.

retrieval methods (LMF, MF and ILMF). In combination with the method for quantifying point source emission rates, the data from Simulation 2 and Simulation 3 can also be utilized to analyze the effect of the ΔXCH_4 retrieval methods on the estimated emission rates.

2.5. WRF-LES

WRF-LES has the capability to simulate realistic three-dimensional volume mixing ratio enhancements for a given emission rate and meteorological conditions. Two-dimensional methane plumes can be obtained by integrating over the column. The LES model setup for the simulation of plumes is described in Varon et al. (2018). Fig. 8 shows an example of a methane plume for an emission rate of 2000 kg/h and a 10 m wind speed of 3 m/s. The emission rate is set by scaling the total methane mass in the plume.

2.6. LBLRTM

The reflected solar radiances were generated by Line-By-Line Radiative Transfer Model (LBLRTM) (Clough et al., 2005; Dennison et al., 2013; Liu et al., 2023). The line parameter database was built from HITRAN 2012. And the LBLRTM solar inputs were generated with the "extract solar" function available on the AER RT website and the Kurucz solar source function. The 1976 U.S. Standard Atmosphere (including temperature, pressure, and other gas concentrations) (Anderson et al., 1986) was used for all cases except for the methane concentration. The air column was divided into 42 layers and the two-way transmittance was assumed for all layers.

These parameters such as SZA, VZA, etc. can be used as inputs for the radiative transfer model to simulate reflected solar radiance. Further, the radiances can be used to retrieve concentration enhancements using MF or LMF.

2.7. Methods for quantifying point source emission rates from observations of column plumes

The characteristics of methane plumes depend mainly on the intensity of the emission source and the wind speed. Methods commonly used to quantify point source rates from plumes include the integrated mass enhancement(IME) (Frankenberg et al., 2016; Thompson et al., 2016), the Gaussian plume inversion method (Zheng et al., 2020; Shi et al., 2023), the cross-sectional flux method (Conley et al., 2016), and the source pixel method (Jacob et al., 2016). These methods were compared in a previous study and the IME was better adapted to the problem (Varon et al., 2018). The relationship between U_{eff} and U_{10} and the evaluation of IME precision are referred to Guanter et al. (Guanter et al., 2021). The local wind speed data is obtained from GEOS-FP dataset. The error propagation scheme is referred to Cusworth et al. (2020).

Table 2
Comparison of MF and LMF methods.

Cases	MF		LMF	
	Result (ppb)	bias(%)	Result (ppb)	bias(%)
Case 2	98.59	−1.41	100.02	0.02
Case 3	550.76	−8.21	599.73	−0.05
Case 4	946.10	−14.00	1099.66	−0.03
Case 5	1295.34	−19.04	1599.82	−0.01
Case 6	1606.67	−23.50	2100.10	0.004

2.8. Data sources

The real data used in this work are from the imaging spectrometer onboard Italian PRISMA mission (Cogliati et al., 2021). PRISMA captures hyperspectral images in the wavelength range of 400 to 2500 nm with a spatial sampling of 30 m using a push broom mode and provides freely accessible data to the scientific community upon request.

3. Results

3.1. Performance comparison between MF and LMF

We designed 6 Cases with the same H1 of 100 km, H2 of 0 km, VZA of 0°, SZA of 30°, and different column concentrations of 1900 ppb, 2000 ppb, 2500 ppb, 3000 ppb, 3500 ppb, and 4000 ppb. The methane background concentration was always considered to be 1900 ppb. In other words, Case 1 was used to generate the reference spectrum. Cases 2–6 were used to generate the spectrums affected by the methane, with known enhancements of 100 ppb, 600 ppb, 1100 ppb, 1600 ppb, and 2100 ppb, respectively. The objective of this section is to compare the MF and the LMF performance using ideal observations, which can be obtained with simulated data with no instrument noise, no interference from trace gases as H_2O and CO_2, and no spectral convolution being applied. The performances in simulated experiments are shown in Table 2. The MF method consistently underestimates the concentration enhancement. And the bias of the MF increases as the concentration enhancement increases. The bias is up to 23.5% for a concentration enhancement of 2100 ppb. In contrast, the bias of LMF is always below 0.05% for all concentration enhancements.

3.2. Result from Simulation 1

The random simulated enhancement can show the performance of each method over a large methane enhancement range and with a uniform sampling. Fig. 9 shows the scatter plot comparing the true and the retrieved concentration enhancements over the enhanced pixels. Linear regression lines and reference lines with a slope of 1 are plotted along with the scatter points. In addition, R^2, bias, root-mean-square error

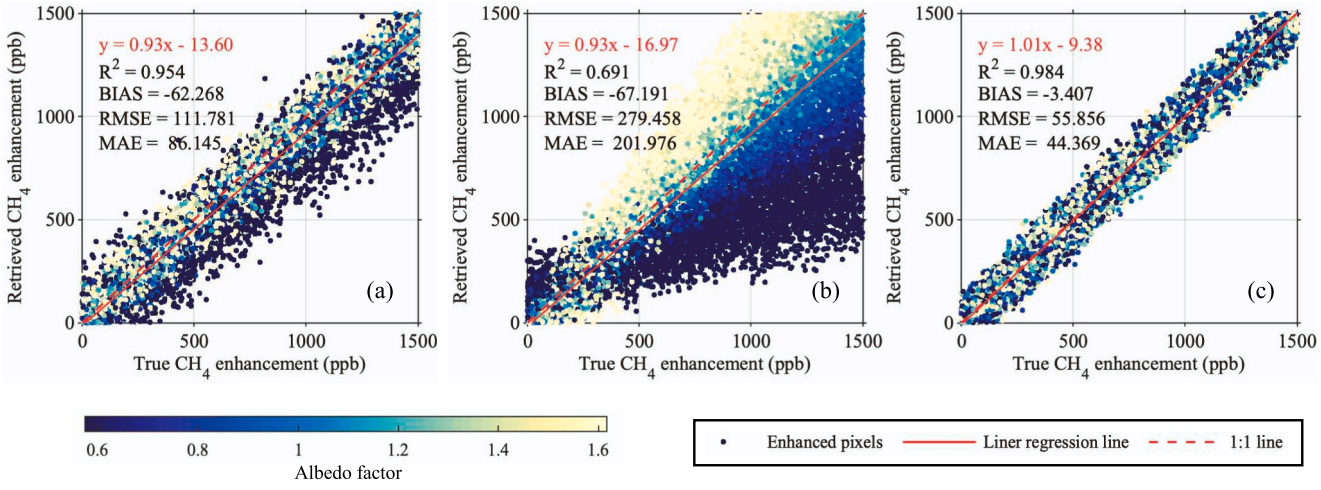

Fig. 9. Scatterplots comparing true ΔCH_4 enhancements and retrieved CH_4 enhancements for randomly simulated enhancements varying from 0 to 1500 ppb. (a) to (c) represents LMF, MF, and ILMF respectively. Only enhanced pixels are shown here. Points are colored according to the true albedo factors. The solid red line is the linear regression of these scattered points. The red dashed line is the line with a slope of 1. (For interpretation of the references to colour in this figure legend, the reader is referred to the web version of this article.)

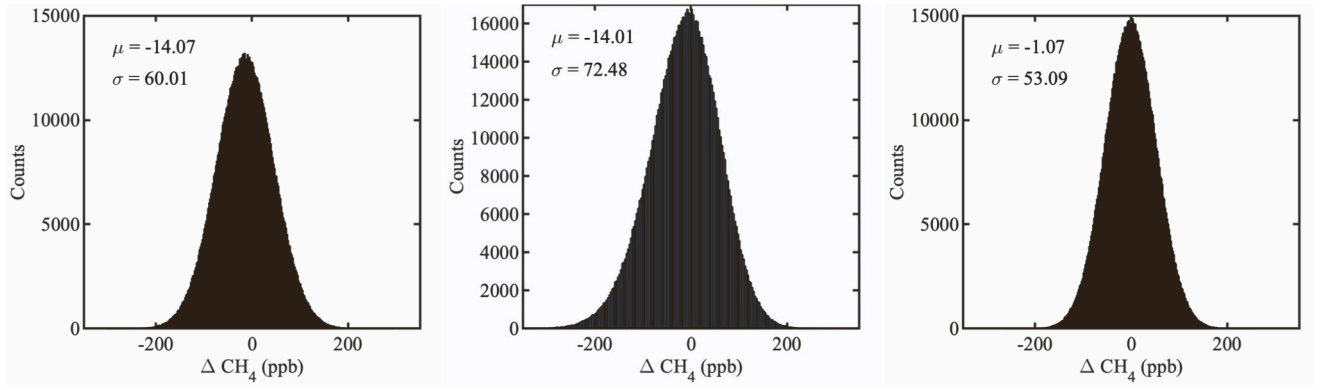

Fig. 10. Histograms of the retrieved ΔCH_4 for the unenhanced pixels from the random enhancement simulation. (a) to (c) represents LMF, MF, and ILMF respectively. The mean and standard deviation are shown in the panel.

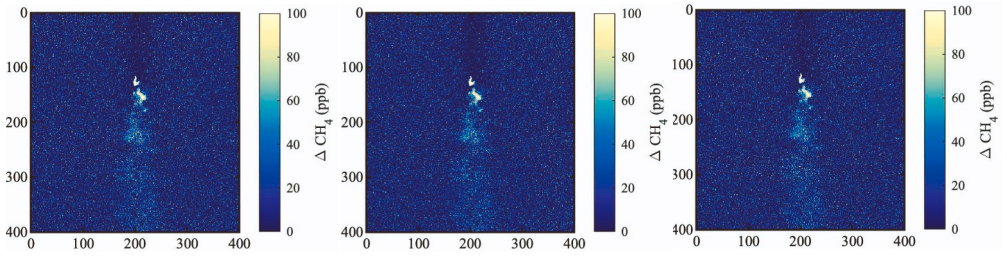

Fig. 11. Retrieved methane plumes using three methods for emission rates of 2000 kg/h, with instrument precision σ of 1%. (a) to (c) represents LMF, MF, and ILMF respectively.

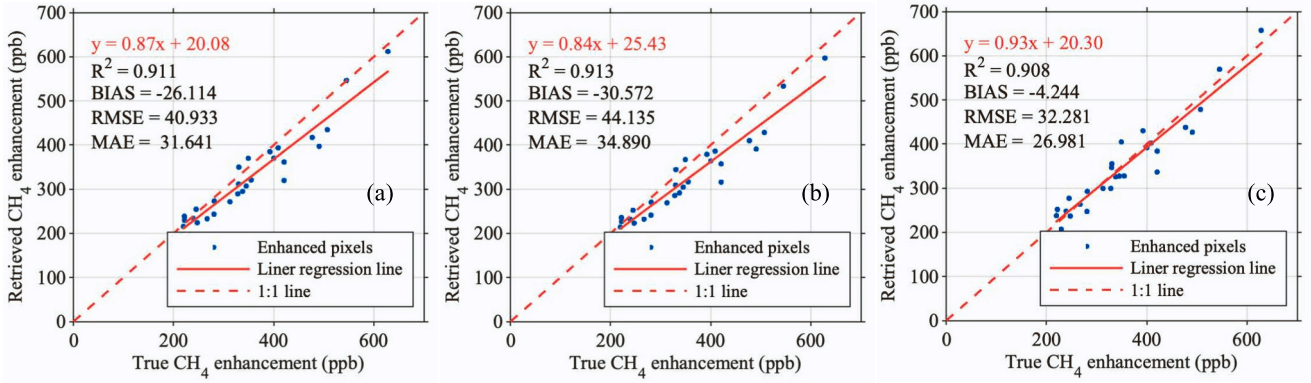

Fig. 12. Scatterplots comparing true CH_4 enhancements and retrieved CH_4 enhancements, with emission rate of 1000 kg/h. (a) to (c) represents LMF, MF, and ILMF respectively. Only enhanced pixels are shown here. The solid red line is the linear regression of these scattered points. The red dashed line is the line with a slope of 1. (For interpretation of the references to colour in this figure legend, the reader is referred to the web version of this article.)

(RMSE) and mean-absolute-error (MAE) are also illustrated respectively. From multiple evaluation metrics, the ILMF method is the best and the MF method is the worst among the three methods. The best bias is achieved by the ILMF with a relative improvement over the reference MF of 94.9%. The best RMSE is also achieved by the ILMF with a relative improvement over the reference MF of 80%. LMF and ILMF have similar R^2, but the deviation and RMSE of LMF are higher, which is due to some enhanced pixels with a low surface albedo (See dark scatters in Fig. 9 (a)). The underestimation due to this reason is more obvious in the MF method (See dark scatters in Fig. 9 (b)).

The methane concentration enhancement retrievals for the non-enhanced pixels is shown in Fig. 10. The variation in the retrieved concentration enhancement on unenhanced pixels can be used to evaluate the retrieval presicion (Guanter et al., 2021). The unenhanced pixels retrieved by the ILMF have the closest mean to zero and the smallest standard deviation.

3.3. Result from Simulation 2

The concentration enhancement images simulated by the WRF-LES model can be used not only to compare the input concentration enhancement with the retrieved concentration enhancement but also can be further used to evaluate the performance of the method in quantifying the emission rates of point sources. Unlike the random simulated concentration enhancements that conform to a uniform distribution, most of the concentration enhancement generated by WRF-LES is around 0 ppb. Only a very few pixels near the emission source appear to have large concentration enhancements. The retrieved plume is clearly visible in the image for each method (see Fig. 11). However, the visual judgment of the plume will become more difficult for small

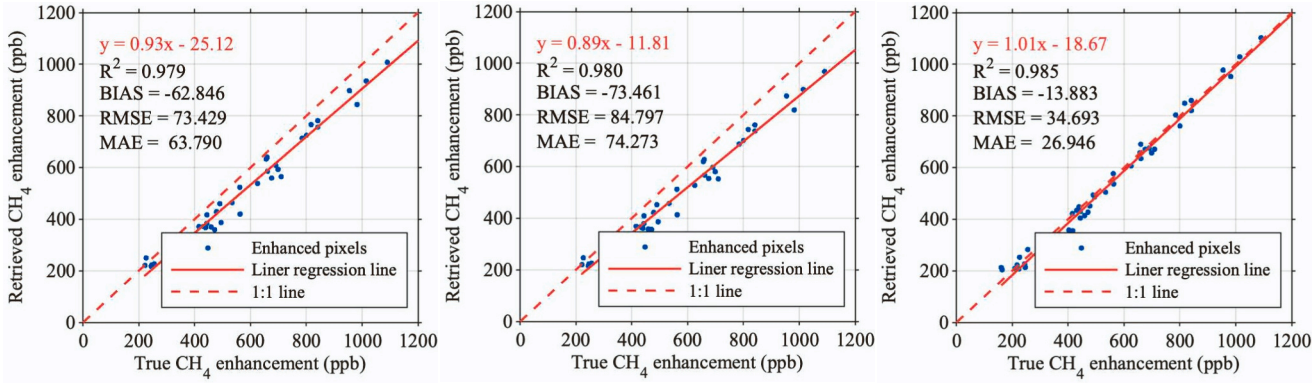

Fig. 13. Scatterplots comparing true CH_4 enhancements and retrieved CH_4 enhancements, with emission rate of 2000 kg/h. (a) to (c) represents LMF, MF, and ILMF respectively. Only pixels with a concentration enhancement >200 ppb are shown here. The solid red line is the linear regression of these scattered points. The red dashed line is the line with a slope of 1. (For interpretation of the references to colour in this figure legend, the reader is referred to the web version of this article.)

Table 3
Retrieved emission rates (Q) of three methods.

True Q (kg/h)	Retrieved Q (kg/h)		
	LMF	MF	ILMF
1000	970±13	967±13	985±13
2000	1902±15	1884±14	1987±16

emission rates due to the instrument noise.

To more clearly demonstrate the improvement for large concentration enhancement retrievals, Fig. 12 and Fig. 13 show the scatter plot for concentration enhancements >200 ppb. Fig. 12 and Fig. 13 represent the method performance for emission rates of 1000 kg/h and 2000 kg/h, respectively. Both scatter plots demonstrate the underestimation of MF for large concentration enhancements, which will inevitably lead to further underestimation of emission rates.

We used the IME method introduced in Section 2.7 to estimate the emission rates from the retrieved methane concentration enhancement images. The procedure for constructing the plume mask refers to Varon et al. (2018). Instrument precision (σ = 1%) was considered and the experiment was repeated 100 times. The result is shown in Table. 3. As with the previously shown scatter plots, MF underestimates the emission rate more than the other two methods (LMF and ILMF) whether at 1000 kg/h or 2000 kg/h. The degree of underestimation is 3.3% and 5.8%, respectively. Although ILMF also suffers from underestimation, it has improved its accuracy by 1.8% and 5.15% compared to MF.

3.4. Result from Simulation 3

Fig. 14 presents the results of end-to-end simulations for the four selected locations, where clear plumes can be observed on the retrieved ΔXCH_4 maps. However, the visible plumes are incomplete compared to those shown in Fig. 11, limited only to higher concentrations.

It is important to note that the plume mask greatly affects the estimate of the source rate. Actually, the masked plume as an IME input is hardly an accurate representation of the true plume. Even on a homogeneous surface, plume edges with small concentration enhancements may be confused with the instrument noise. For smaller emission point sources, less enhanced pixels can be used as the input of IME method, which will bring great uncertainty to the estimation of emission rate. A statistically significant methane enhancement is generally considered greater than twice the standard deviation, which is known as significance test. However, there may also be statistically significant retrieval artifacts near the plume due to the surface type. These random classification errors can be addressed through median filter, followed by Gaussian filter and thresholding (Varon et al., 2018). Fig. 15 shows two examples of the mask-constructing procedure. If retrieval artifacts are inside the plume, this unexpected effect is difficult to eliminate. If the plume along the wind direction appear over homogeneous surface, fortunately, then a more accurate emission rate can be obtained.

Additionally, we investigated the performance of the MF method and the ILMF method in estimating emissions from four locations and ten emission rates. A comparison between the retrieved Q values and the true Q values can be seen in Fig. 16. The retrieved emission rates were generally underestimated, regardless of whether the MF or the ILMF method was used. The underestimation typically resulted from two factors: first, the enhancement of the retrieved concentrations was underestimated, and second, large fractions of the true plume can not be captured in PRISMA-derived ΔXCH_4 map. For higher emission rates (6000–10,000 kg/h), the MF method showed larger underestimation than the ILMF method at all four locations, due to the underestimation of retrieved concentration enhancement. The degree of underestimation decreased as the emission rates decreased. For example, in Algeria, the retrieved Q based on the MF method were underestimated by 32% and 15% for emission rates of 8000 kg/h and 5000 kg/h, respectively. In addition, low emission rates resulted in fewer statistically significant plume pixels, making it difficult to provide reliable estimates of emission rates. For a Q value of 2000 kg/h at the China site, as shown in Fig. 16, the ILMF method showed significant underestimation. However, this underestimation was due to few plume pixels, as shown in Fig. 15. For a Q value of 1000 kg/h at the China site, neither the MF nor ILMF method could retrieve any usable plume pixels after masking.

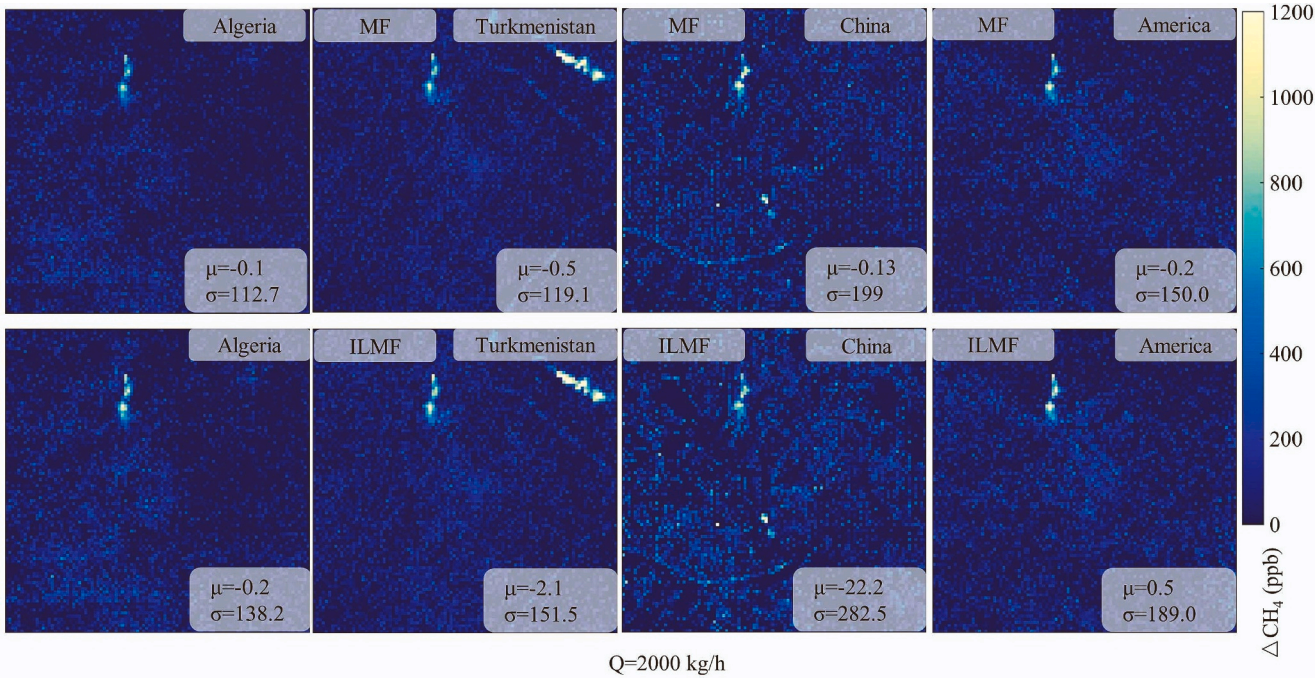

Fig. 14. Retrieved ΔXCH_4 maps from the end-to-end simulations at the four different sites. Top row, retrieved ΔXCH_4 maps (100 × 100 pixels) using MF method. Bottom row, retrieved ΔXCH_4 maps (100 × 100 pixels) using ILMF method. μ and σ in the label on the bottom right corner of each panel refers to the mean and standard deviation for the no-plume pixels.

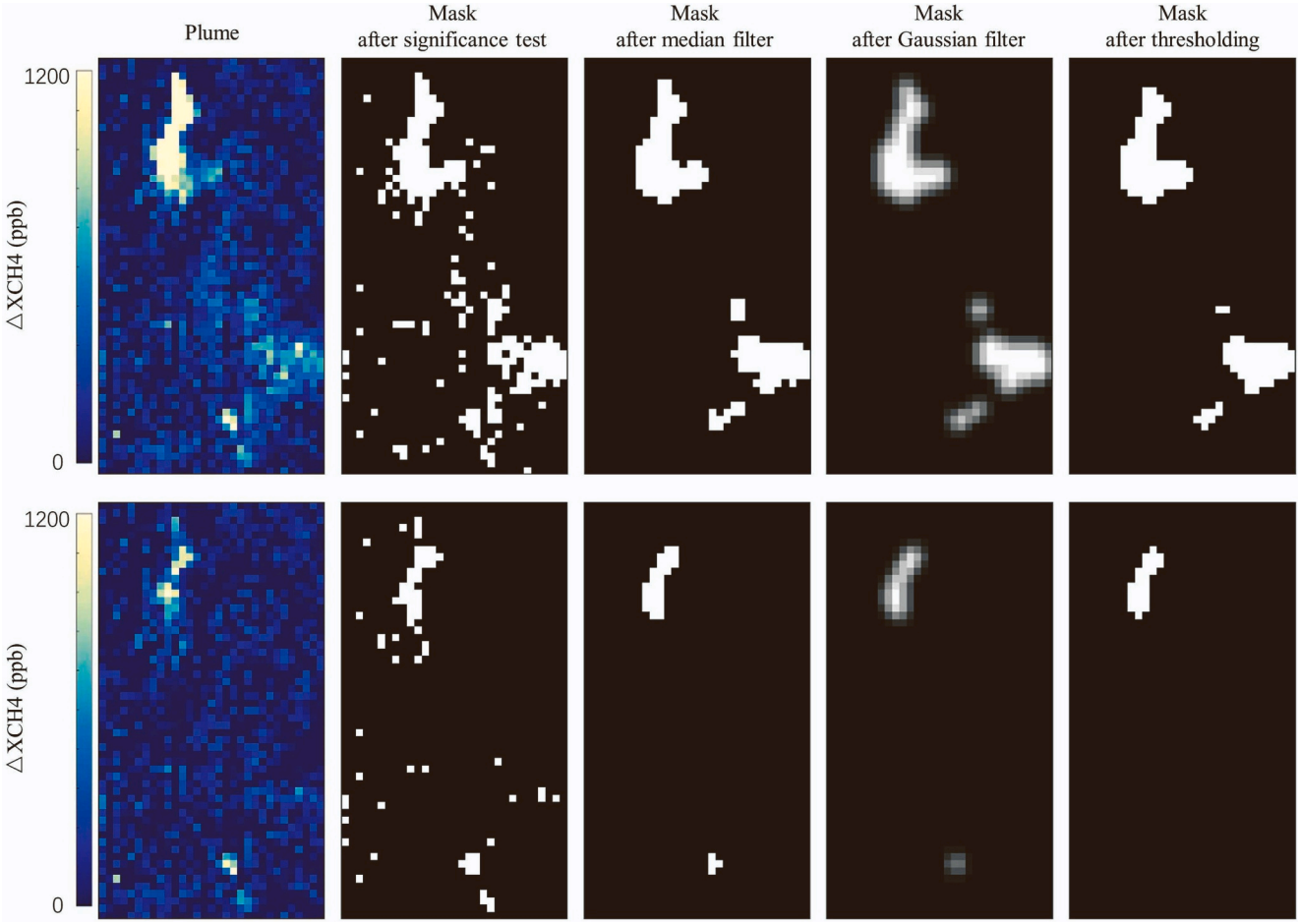

Fig. 15. Procedure illustration for constructing the plume mask. Top row, retrieved ΔXCH_4 map using pseudo-observation from China site for a point source Q = 8000 kg/h, and its corresponding mask constructing procedure. Bottom row, retrieved ΔXCH_4 map using pseudo-observation for a point source Q = 2000 kg/h and its corresponding mask constructing procedure. The last column indicates the final mask.

Furthermore, it is noteworthy that larger underestimation occurred in Algeria, which has a bright and homogeneous surface, rather than in China, which has a dark and heterogeneous surface, at the same emission rate. This is because the heterogeneous and dark surface is more likely to cause retrieval artifacts within the plume, which cannot be filtered out by the filters. These retrieval artifacts within the plume will mitigate the underestimation of emission rates. However, this unexpected effect is difficult to evaluate.

Taking the Algeria site as an example to minimize the ambiguous effect due to the retrieval artifacts, Table 4 shows the separate effects of concentration retrievals on emission rate underestimation. Table 4 shows that the underestimation of emission rates caused by concentration retrieval accounts for about 57% of the total underestimation. This underestimation resulting from this source is <16% for the ILMF method. For a Q value of 10,000 kg/h, the emission rate estimated by the ILMF method has an accuracy improvement of 16.4% compared to the MF method.

3.5. Results from real data

Table 5 demonstrates the emission rates from the 14 methane emitters retrieved with PRISMA. Compared with the emission rates using the MF method, ILMF consistently estimates a greater emission rate than MF. The underestimation of the emission rate for MF comes from the underestimation of the ΔXCH_4 image, which is attributed to the first-order Taylor expansion of Beer lambert law. Some examples of retrieved methane plumes from real PRISMA images are shown in Fig. 17. Two plumes are clearly visible in Fig. 17 (a), which originate from two oil and gas production sites by viewing high-resolution optical images from Google Earth. The plumes in Fig. 17 (b) and (c) are caused by coal mines. They are both located in Shanxi province, which is one of the highest coal producing provinces in China. The plumes in Fig. 17 (d) comes from the Permian Basin, one of the largest oil and gas producing regions in the United States (Cusworth et al., 2021a). A series of experiments have been conducted here to investigate methane leaks (Chen et al., 2022; Irakulis-Loitxate et al., 2021). Many false positives are clearly visible in the raw images, especially in Shanxi and Permian Basin. Most of the false positives are caused by the spectral overlap of surface absorption properties with methane absorption in the retrieval window. These false positives can be further determined by combining local wind direction and high resolution optical images.

4. Conclusions

This study revealed the underestimation of the traditional MF method in quantifying methane emission point sources, especially for strong plumes. We proposed an ILMF to quantify emissions unbiasedly. The iterative use of filters can deal with the accurate estimation of mean and covariance under the circumstance of a large proportion of enhanced pixels. In addition, we employed the ideal pixel-level simulation and three image-level simulations to comprehensively assess the performance of the different retrieval methods. Lastly, we applied ILMF in real data retrieval to estimate emission rates in four countries.

The ideal pixel-level simulation experiments demonstrated that the

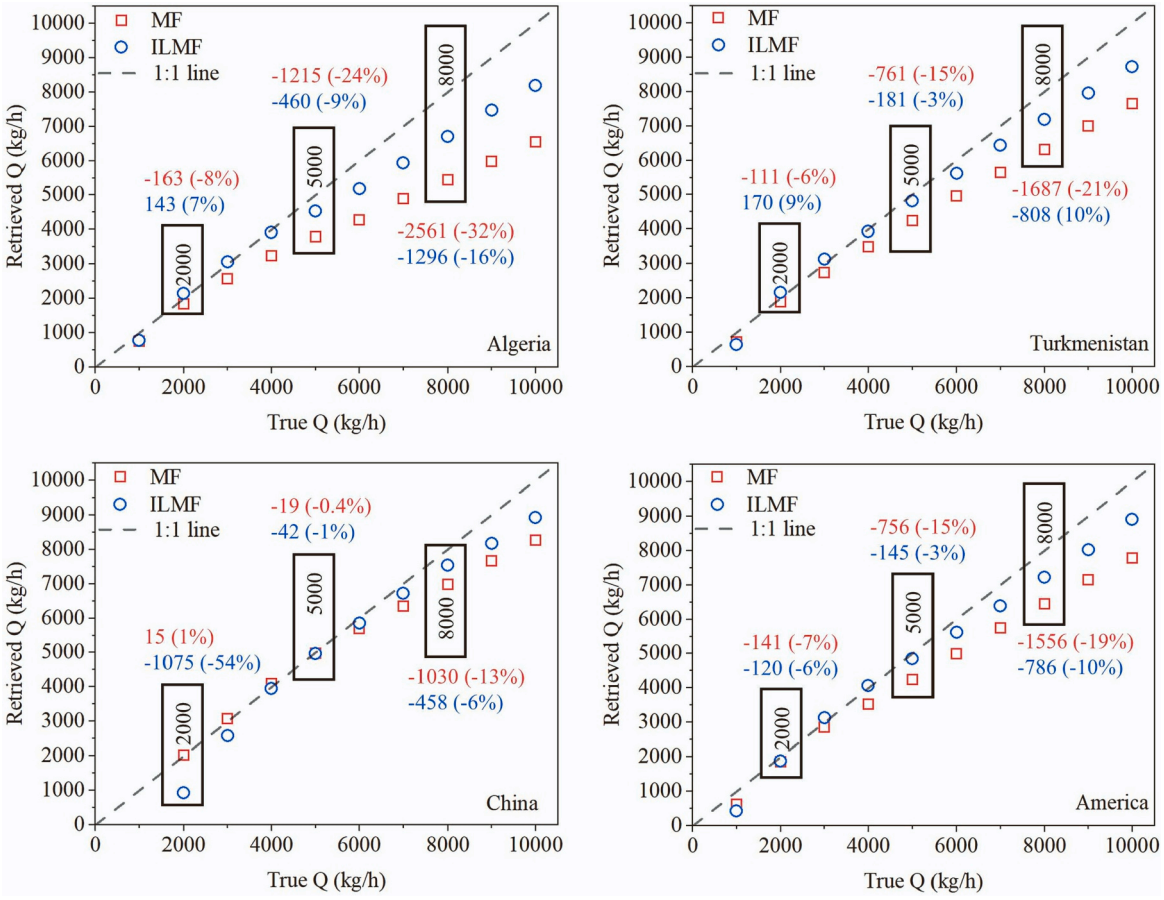

Fig. 16. Scatterplots comparing true Q and retrieved Q. For Q 2000 kg/h, Q 5000 kg/h, and Q 8000 kg/h, the errors of MF and ILMF are labeled. The black line is the line with a slope of 1.

Table 4
Comparison of the true Q with the retrieved Q(MF) and the retrieved Q(MF_Ref) for the Algeria site. Q(MF) and Q(ILMF) represent the estimated Q obtained by the MF and ILMF methods, respectively, combined with their respective masks. Q(MF_Ref) represents the estimated Q based on the true ΔXCH_4 and the mask derived from MF method. Q(ILMF_Ref) represent the estimated Q based on the true ΔXCH_4 and the mask derived from ILMF method. Proportion (%) indicates the proportion of total underestimation caused by concentration retrieval.

True Q (kg/h)	Q(MF) (kg/h)	Q(MF_Ref) (kg/h)	Proportion (%)	Q(ILMF) (kg/h)	Q(ILMF_Ref) (kg/h)	Proportion (%)
6000	4273	5283	58.5	5179	5181	0.3
7000	4887	6099	57.4	5934	6001	6.3
8000	5438	6902	57.1	6703	6864	12.4
9000	5976	7704	57.2	7467	7654	12.2
10,000	6539	8517	57.2	8178	8463	15.7

Table 5
Emission rates from 14 methane emitters retrieved with PRISMA.

	Date	Country	Latitude	Longitude	Emission Rate Estimates (kg/h)	
					MF	ILMF
Emitter 1	2020/08/30	Algeria	31.778°N	5.995°E	3840±1540	3900±1560
Emitter 2	2020/08/30	Algeria	31.767°N	5.997°E	2790±1116	3010±1204
Emitter 3	2021/02/06	China	36.233°N	112.945°E	12,010±4800	12,850±5140
Emitter 4	2021/02/06	China	36.246°N	112.990°E	14,020±5600	14,730±5900
Emitter 5	2021/02/17	United States	32.205°N	103.715°W	2080±830	2370±950
Emitter 6	2021/07/31	Turkmenistan	36.474°N	61.459°°E	1630±652	2561±1024
Emitter 7	2021/07/31	Turkmenistan	36.413°N	61.476°°E	953±381	1323±529
Emitter 8	2021/07/31	Turkmenistan	36.511°N	61.650°°E	490±196	691±276
Emitter 9	2021/07/31	Turkmenistan	36.511°N	61.661°°E	614±245	902±361
Emitter 10	2021/08/19	Algeria	31.798°N	6.011°E	5781±2312	7241±2896
Emitter 11	2021/08/19	Algeria	31.806°N	6.142°E	1137±454	1314±526
Emitter 12	2021/08/19	Algeria	31.806°N	6.155°E	1476±590	1634±654

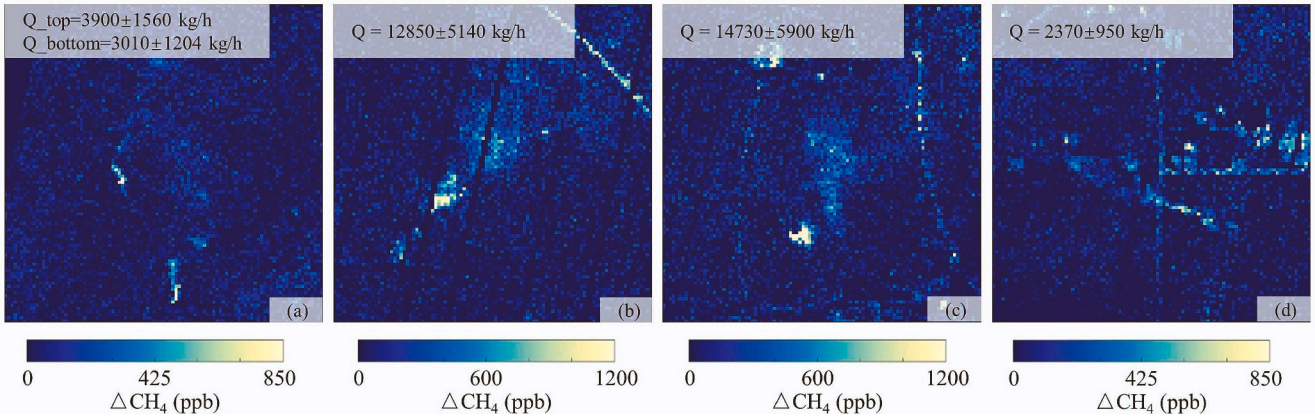

Fig. 17. Retrieved ΔXCH_4 maps from the real PRISMA images using ILMF method. (a) Emitters from Algeria on 30 August 2020 with 2 plumes (31.778°N, 5.995°E and 31.767°N, 5.997°E). (b) Emitter from Shanxi in China on 6 February 2021 (36.233°N, 112.945°E). (c) Emitter from Shanxi in China on 6 February 2021 (36.246°N, 112.990°E). (d) Emitter from Permian Basin in USA on 17 February 2021 (32.205°N, 103.715°W).

MF method lead to an underestimated methane concentration enhancement, which was up to 23.5% for a concentration enhancement of 2100 ppb. In the image-level Simulation 1, the concentration enhancements retrieved by ILMF matched best with the true enhancement, with an R^2 of 0.984 and a small RMSE of 55.856 ppb. The relative improvements in bias and RMSE reached 94.9% and 80%, respectively, compared to the reference MF method. In the image-level Simulation 2, the ΔXCH_4 images retrieved by LMF, MF and ILMF were visually similar, but the concentration enhancement over a few highly enhanced pixels were underestimated by MF. As a result, emission rates of 1000 kg/h and 2000 kg/h were underestimated by 3.3% and 5.8% by the MF method. In the image-level Simulation 3, the performance of ILMF was evaluated in four different methane hotspot regions. In the context of ideal surface observations, the MF method tends to underestimate emission rates due to two factors, with underestimation caused by concentration retrieval accounting for approximately 57%. This underestimation can be addressed by utilizing the ILMF method proposed in this study. However, the underestimation caused by plume edge omissions still remains a challenge. Since the retrieval precision affects the size of the mask, it is necessary to further investigate the effect of retrieval precision on the emission rate estimating. It is noteworthy that the presence of retrieval artifacts in the plume can lead to an overestimation of the emission rates, which is more likely to occur on heterogeneous surfaces. In other words, the underestimation of emission rates due to concentration retrieval and plume edge omission would be unquantifiably mitigated. Findings from our simulation experiments provides compelling evidence of a systemic underestimation inherent to the MF method, spanning both concentration retrieval and emission rate estimation. Notably, our analysis reveals a concerning trend whereby the magnitude of underestimation amplifies in tandem with higher concentration enhancements. These insights emphasize the critical importance of robust and accurate concentration retrieval method for quantifing methane point sources.

The results from the real data confirm the dependence of the retrieval on the surface type. Bright and homogeneous surfaces in Algeria and Turkmenistan facilitate the detection of plumes. A careful visual inspection is required to distinguish a large number of potential false positives on heterogeneous surfaces. The concentration enhancement of true plume gradually decreases along the direction of wind speed, while the false plume is similar with the shape of the specific surface type.

Our results demonstrate the great potential of PRISMA-like satellites for the detection and quantification of methane point sources, especially on bright and homogeneous surfaces. Our proposed ILMF method effectively addresses the issue of systematic underestimation of concentration enhancement that is commonly associated with traditional MF method. This novel method offers a more accurate and reliable means of assessing concentration enhancement, thus providing accurate input for quantifying emission rates.

CRediT authorship contribution statement

Zhipeng Pei: Conceptualization, Data curation, Investigation, Methodology, Software, Visualization, Writing - original draft, Writing - review & editing. Ge Han: Funding acquisition, Supervision, Writing - review & editing. Huiqin Mao: Supervision, Data curation, Investigation. Cuihong Chen: Supervision, Data curation, Investigation. Tianqi Shi: Formal analysis, Validation. KeyiYang: Software. Xin Ma: Supervision. Wei Gong: Supervision.

Declaration of Competing Interest

The authors declare that they have no known competing financial interests or personal relationships that could have appeared to influence the work reported in this paper.

Data availability

Data will be made available on request.

Acknowledgement

This study was funded by National key research and development program (Grant No. 2022YFB3904801), National Natural Science Foundation of China (Grant No. 4197283, 41827801), the Fundamental Research Funds for the Central Universities (2042023kf1050). The authors would like to thank the Italian Space Agency for the free PRISMA data used in this study. Daniel J. Varon (Harvard University), Markus D. Foote (University of Utah), and Brian Blaylock (University of Utah) are also thanked for helpful discussion and technical assistance. The numerical calculations in this study have been done on the supercomputing system in the Supercomputing Center of Wuhan University.

Appendix A. Supplementary data

Supplementary data to this article can be found online at https://doi.org/10.1016/j.rse.2023.113652.

References

Anderson, G.P., Clough, S.A., Kneizys, F., Chetwynd, J.H., Shettle, E.P., 1986. AFGL atmospheric constituent profiles (0.120 km). Air Force Geophysics Lab Hanscom AFB MA.

Ayasse, A.K., Dennison, P.E., Foote, M., Thorpe, A.K., Joshi, S., Green, R.O., Duren, R.M., Thompson, D.R., Roberts, D.A., 2019. Methane mapping with future satellite imaging spectrometers. Remote Sens. 11, 3054.
Bradley, E.S., Leifer, I., Roberts, D.A., Dennison, P.E., Washburn, L., 2011. Detection of marine methane emissions with aviris band ratios. Geophys. Res. Lett. 38.
Buchwitz, M., Burrows, J.P., 2004. Retrieval of ch4, co, and co2 total column amounts from sciamachy near-infrared nadir spectra: Retrieval algorithm and first results. In: Remote Sensing of Clouds and the Atmosphere VIII. SPIE, pp. 375–388.
Chen, Y., Sherwin, E.D., Berman, E.S., Jones, B.B., Gordon, M.P., Wetherley, E.B., Kort, E. A., Brandt, A.R., 2022. Quantifying regional methane emissions in the New Mexico permian basin with a comprehensive aerial survey. Environ. Sci. Technol. 56, 4317–4323.
Clough, S., Shephard, M., Mlawer, E., Delamere, J., Iacono, M., Cady-Pereira, K., Boukabara, S., Brown, P., 2005. Atmospheric radiative transfer modeling: a summary of the aer codes. J. Quant. Spectrosc. Radiat. Transf. 91, 233–244.
Cogliati, S., Sarti, F., Chiarantini, L., Cosi, M., Lorusso, R., Lopinto, E., Miglietta, F., Genesio, L., Guanter, L., Damm, A., et al., 2021. The prisma imaging spectroscopy mission: overview and first performance analysis. Remote Sens. Environ. 262, 112499.
Conley, S., Franco, G., Faloona, I., Blake, D.R., Peischl, J., Ryerson, T., 2016. Methane emissions from the 2015 aliso canyon blowout in los Angeles, ca. Science 351, 1317–1320.
Cusworth, D.H., Duren, R.M., Thorpe, A.K., Olson-Duvall, W., Heckler, J., Chapman, J. W., Eastwood, M.L., Helmlinger, M.C., Green, R.O., Asner, G.P., et al., 2021. a. Intermittency of large methane emitters in the permian basin. Environ. Sci. Technol. Lett. 8, 567–573.
Cusworth, D.H., Duren, R.M., Thorpe, A.K., Pandey, S., Maasakkers, J.D., Aben, I., Jervis, D., Varon, D.J., Jacob, D.J., Randles, C.A., 2021. Multisatellite imaging of a gas well blowout enables quantification of total methane emissions. Geophys. Res. Lett. 48, e2020GL090864.
Cusworth, D.H., Duren, R.M., Thorpe, A.K., Tseng, E., Thompson, D., Guha, A., Newman, S., Foster, K.T., Miller, C.E., 2020. Using remote sensing to detect, validate, and quantify methane emissions from California solid waste operations. Environ. Res. Lett. 15, 054012.
Cusworth, D.H., Jacob, D.J., Varon, D.J., Chan Miller, C., Liu, X., Chance, K., Thorpe, A. K., Duren, R.M., Miller, C.E., Thompson, D.R., et al., 2019. Potential of next-generation imaging spectrometers to detect and quantify methane point sources from space. Atmos. Meas. Tech. 12, 5655–5668.
Dennison, P.E., Thorpe, A.K., Pardyjak, E.R., Roberts, D.A., Qi, Y., Green, R.O., Bradley, E.S., Funk, C.C., 2013. High spatial resolution mapping of elevated atmospheric carbon dioxide using airborne imaging spectroscopy: radiative transfer modeling and power plant plume detection. Remote Sens. Environ. 139, 116–129.
Duren, R.M., Thorpe, A.K., Foster, K.T., Rafiq, T., Hopkins, F.M., Yadav, V., Bue, B.D., Thompson, D.R., Conley, S., Colombi, N.K., et al., 2019. California's methane super-emitters. Nature 575, 180–184.
Ehret, T., De Truchis, A., Mazzolini, M., Morel, J.M., D'aspremont, A., Lauvaux, T., Duren, R., Cusworth, D., Facciolo, G., 2022. Global tracking and quantification of oil and gas methane emissions from recurrent sentinel-2 imagery. Environ. Sci. Technol. 56, 10517–10529.
EPA, 2022. Understanding global warming potentials. https://www.epa.gov/ghgemissions/understanding-global-warming-potentials. Accessed October 14, 2022.
Foote, M.D., Dennison, P.E., Thorpe, A.K., Thompson, D.R., Jongaramrungruang, S., Frankenberg, C., Joshi, S.C., 2020. Fast and accurate retrieval of methane concentration from imaging spectrometer data using sparsity prior. IEEE Trans. Geosci. Remote Sens. 58, 6480–6492.
Frankenberg, C., Meirink, J.F., van Weele, M., Platt, U., Wagner, T., 2005. a. Assessing methane emissions from global space-borne observations. Science 308, 1010–1014.
Frankenberg, C., Platt, U., Wagner, T., 2005. b. Iterative maximum a posteriori (imap)-doas for retrieval of strongly absorbing trace gases: model studies for ch 4 and co 2 retrieval from near infrared spectra of sciamachy onboard envisat. Atmos. Chem. Phys. 5, 9–22.
Frankenberg, C., Thorpe, A.K., Thompson, D.R., Hulley, G., Kort, E.A., Vance, N., Borchardt, J., Krings, T., Gerilowski, K., Sweeney, C., 2016. Airborne methane remote measurements reveal heavy-tail flux distribution in four corners region. Proc. Natl. Acad. Sciences 113, 9734–9739.
Gorroño, J., Varon, D.J., Irakulis-Loitxate, I., Guanter, L., 2022. Understanding the potential of sentinel-2 for monitoring methane point emissions. Atmos. Meas. Tech. Discuss. 1–25.
Guanter, L., Irakulis-Loitxate, I., Gorroño, J., Sánchez-Garca, E., Cusworth, D.H., Varon, D.J., Cogliati, S., Colombo, R., 2021. Mapping methane point emissions with the prisma spaceborne imaging spectrometer. Remote Sens. Environ. 265, 112671.
Irakulis-Loitxate, I., Guanter, L., Liu, Y.N., Varon, D.J., Maasakkers, J.D., Zhang, Y., Chulakadabba, A., Wofsy, S.C., Thorpe, A.K., Duren, R.M., 2021. Satellite-based survey of extreme methane emissions in the permian basin. Sci. Adv. 7, eabf4507.
Irakulis-Loitxate, I., Guanter, L., Maasakkers, J.D., Zavala-Araiza, D., Aben, I., 2022. Satellites detect abatable super-emissions in one of the world's largest methane hotspot regions. Environ. Sci. Technol. 56, 2143–2152.
Jacob, D.J., Turner, A.J., Maasakkers, J.D., Sheng, J., Sun, K., Liu, X., Chance, K., Aben, I., McKeever, J., Frankenberg, C., 2016. Satellite observations of atmospheric methane and their value for quantifying methane emissions. Atmos. Chem. Phys. 16, 14371–14396.
Jacob, D.J., Varon, D.J., Cusworth, D.H., Dennison, P.E., Frankenberg, C., Gautam, R., Guanter, L., Kelley, J., McKeever, J., Ott, L.E., et al., 2022. Quantifying methane emissions from the global scale down to point sources using satellite observations of atmospheric methane. Atmos. Chem. Phys. Discuss. 1–44.
Jervis, D., McKeever, J., Durak, B.O., Sloan, J.J., Gains, D., Varon, D.J., Ramier, A., Strupler, M., Tarrant, E., 2021. The ghgsat-d imaging spectrometer. Atmos. Meas. Tech. 14, 2127–2140.
Kim, K.E., Lee, S.S., Baik, H.S., 2016. Iterative matched filtering for detection of non-rare target materials in hyperspectral imagery. In: Image and Signal Processing for Remote Sensing XXII. SPIE, pp. 133–139.
Kochanov, R.V., Gordon, I., Rothman, L., Wciso, P., Hill, C., Wilzewski, J., 2016. Hitran application programming interface (hapi): a comprehensive approach to working with spectroscopic data. J. Quant. Spectrosc. Radiat. Transf. 177, 15–30.
Liu, B., Ma, X., Guo, J., Li, H., Jin, S., Ma, Y., Gong, W., 2023. Estimating hub-height wind speed based on a machine learning algorithm: implications for wind energy assessment. Atmos. Chem. Phys. 23, 3181–3193.
Masson-Delmotte, V., Zhai, P., Pirani, A., Connors, S.L., Péan, C., Berger, S., Caud, N., Chen, Y., Goldfarb, L., Gomis, M., 2021. Climate change 2021: the physical science basis. In: Contribution of Working Group I to the Sixth Assessment Reportof the Intergovernmental Panel on Climate Change 2.
Naik, V., Szopa, S., Adhikary, B., Artaxo, P., Berntsen, T., Collins, W.D., Fuzzi, S., Gallardo, L., Kiendler Scharr, A., Klimont, Z., Liao, H., Unger, N., and Zanis, P. Short-Lived Climate Forcers, in: Climate Change 2021: The Physical Science Basis. Contribution of Working Group I to the Sixth Assessment Report of the Intergovernmental Panel on Climate Change, edited by: Masson-Delmotte, V., Zhai, P., Pirani, A., Connors, S.L., Péan, C., Berger, S., Caud, N., Chen, Y., Goldfarb, L., Gomis, M. L., Huang, M., Leitzell, K., Lonnoy, E., Matthews, J.B.R., Maycock, T.K., Waterfield, T., Yelekçi, O., Yu, R., and Zhou, B., Cambridge University Press, https://www.ipcc.ch/report/ar6/wg1/downloads/report/IPCC_AR6_WGI_Chapter06.pdf.
Ramier, A., Deglint, H., Gains, D., Jervis, D., McKeever, J., Shaw, W., Strupler, M., Tarrant, E., Varon, D.J., 2020. GHGSat-C1-Initial Results, Design, and Characterization, in: AGU Fall Meeting Abstracts. A247-03.
Roberts, D.A., Bradley, E.S., Cheung, R., Leifer, I., Dennison, P.E., Margolis, J.S., 2010. Mapping methane emissions from a marine geological seep source using imaging spectrometry. Remote Sens. Environ. 114, 592–606.
Sadavarte, P., Pandey, S., Maasakkers, J.D., Lorente, A., Borsdorff, T., Denier van der Gon, H., Houweling, S., Aben, I., 2021. Methane emissions from superemitting coal mines in Australia quantified using tropomi satellite observations. Environ. Sci. Technol. 55, 16573–16580.
Sánchez-Garca, E., Gorroño, J., Irakulis-Loitxate, I., Varon, D.J., Guanter, L., 2022. Mapping methane plumes at very high spatial resolution with the worldview-3 satellite. Atmos. Meas. Tech. 15, 1657–1674.
Saunders, R., Matricardi, M., Brunel, P., 1999. An improved fast radiative transfer model for assimilation of satellite radiance observations. Q. J. R. Meteorol. Soc. 125, 1407–1425.
Scafutto, R.D.M., van der Werff, H., Bakker, W.H., van der Meer, F., de Souza Filho, C.R., 2021. An evaluation of airborne swir imaging spectrometers for ch4 mapping: implications of band positioning, spectral sampling and noise. Int. J. Appl. Earth Obs. Geoinf. 94, 102233.
Schaum, A., 2021. A uniformly most powerful detector of gas plumes against a cluttered background. Remote Sens. Environ. 260, 112443.
Shi, T., Han, G., Ma, X., Mao, H., Chen, C., Han, Z., Pei, Z., Zhang, H., Li, S., Gong, W., 2023. Quantifying factory-scale co2/ch4 emission based on mobile measurements and emission-partition model: cases in China. Environ. Res. Lett. 18, 034028.
Thompson, D., Leifer, I., Bovensmann, H., Eastwood, M., Fladeland, M., Frankenberg, C., Gerilowski, K., Green, R., Kratwurst, S., Krings, T., et al., 2015. Real-time remote detection and measurement for airborne imaging spectroscopy: a case study with methane. Atmos. Meas. Tech. 8, 4383–4397.
Thompson, D., Thorpe, A., Frankenberg, C., Green, R., Duren, R., Guanter, L., Hollstein, A., Middleton, E., Ong, L., Ungar, S., 2016. Space-based remote imaging spectroscopy of the aliso canyon ch4 superemitter. Geophys. Res. Lett. 43, 6571–6578.
Thorpe, A., Frankenberg, C., Roberts, D., 2014. Retrieval techniques for airborne imaging of methane concentrations using high spatial and moderate spectral resolution: application to aviris. Atmos. Meas. Tech. 7, 491–506.
Thorpe, A.K., Frankenberg, C., Aubrey, A., Roberts, D., Nottrott, A., Rahn, T., Sauer, J., Dubey, M., Costigan, K., Arata, C., et al., 2016. Mapping methane concentrations from a controlled release experiment using the next generation airborne visible/infrared imaging spectrometer (aviris-ng). Remote Sens. Environ. 179, 104–115.
Thorpe, A.K., Roberts, D.A., Bradley, E.S., Funk, C.C., Dennison, P.E., Leifer, I., 2013. High resolution mapping of methane emissions from marine and terrestrial sources using a cluster-tuned matched filter technique and imaging spectrometry. Remote Sens. Environ. 134, 305–318.
UNEP, CCAC, 2021. Global methane assessment: Benefits and costs of mitigating methane emissions.
Varon, D.J., Jacob, D.J., McKeever, J., Jervis, D., Durak, B.O., Xia, Y., Huang, Y., 2018. Quantifying methane point sources from fine-scale satellite observations of atmospheric methane plumes. Atmos. Meas. Tech. 11, 5673–5686.
Varon, D.J., Jervis, D., McKeever, J., Spence, I., Gains, D., Jacob, D.J., 2021. High-frequency monitoring of anomalous methane point sources with multispectral sentinel-2 satellite observations. Atmos. Meas. Tech. 14, 2771–2785.
Yang, S., Yang, J., Shi, S., Song, S., Luo, Y., Du, L., 2023. The rising impact of urbanization-caused co2 emissions on terrestrial vegetation. Ecol. Indic. 148, 110079.

Zhang, J., Han, G., Mao, H., Pei, Z., Ma, X., Jia, W., Gong, W., 2022. The spatial and temporal distribution patterns of xch4 in China: new observations from tropomi. Atmosphere 13, 177.
Zhang, Y., Wang, W., He, J., Jin, Z., Wang, N., 2023. Spatially continuous mapping of hourly ground ozone levels assisted by himawari-8 short wave radiation products. GISci. Remote Sens. 60, 2174280.
Zheng, B., Chevallier, F., Ciais, P., Broquet, G., Wang, Y., Lian, J., Zhao, Y., 2020. Observing carbon dioxide emissions over china's cities and industrial areas with the orbiting carbon observatory-2. Atmos. Chem. Phys. 20, 8501–8510.